

Effects of V Alloying on Thermoelectric Properties of NbFeSb Half-Heusler Materials Codoped with Ti, Zr, and Sn

Sung-Jae Joo*, JeongIn Jang, Ji-Hee Son, Bong-Seo Kim, and Bok-Ki Min

Energy Conversion Research Center, Korea Electrotechnology Research Institute, Changwon 51543, Republic of Korea

Abstract: NbFeSb-based alloys are promising *p*-type half-Heusler materials with excellent thermoelectric performance, thermal stability, and naturally abundant constituent elements. Alloying and doping are powerful techniques for enhancing the thermoelectric properties of half-Heusler materials. This study experimentally investigated the effects of V alloying in NbFeSb codoped with Ti, Zr, and Sn. As the V content increases, the electrical conductivity of $\text{Nb}_{0.8-x}\text{V}_x\text{Ti}_{0.15}\text{Zr}_{0.05}\text{FeSb}_{0.98}\text{Sn}_{0.02}$ ($x = 0, 0.05, 0.1, 0.2, \text{ and } 0.3$) decreases monotonically because of a simultaneous reduction in carrier concentration and mobility, reducing the power factor up to -39% from 4.13 ($x = 0$) to $2.52 \text{ mW m}^{-1}\text{K}^{-2}$ ($x = 0.3$) at 298 K . Moreover, the lattice thermal conductivity decreases with increasing x by as much as -40% at the maximum V content of $x = 0.3$, demonstrating that V addition considerably enhances phonon scattering even in the presence of substitutional dopants Ti, Zr, and Sn. The differences in the mass and size of V and Nb atoms cause a substantial decrease in lattice thermal conductivity. According to our study, the addition of a small V content to Hf-free NbFeSb-based alloys can improve their thermoelectric properties, and a maximum dimensionless figure of merit zT of 0.89 was obtained in $\text{Nb}_{0.75}\text{V}_{0.05}\text{Ti}_{0.15}\text{Zr}_{0.05}\text{Sn}_{0.98}\text{Sb}_{0.02}$ at 973 K .

(Received 19 July, 2022; Accepted 18 August, 2022)

Keywords: thermoelectric properties, half-Heusler, NbFeSb, V, thermal conductivity

1. INTRODUCTION

Thermoelectric devices have distinct features such as noiseless operation, small volume, and long-term reliability. The recent interest in ecofriendly power sources is inspiring research on waste heat recovery via thermoelectric generation. Among the promising thermoelectric materials for mid-to-high temperature applications, including skutterudites [1-3] and silicides [4-6], half-Heusler (HH) materials have attracted considerable attention because they show major advantages, such as high performance, mechanical robustness, and thermal stability [7-9]. NbFeSb-based HH compounds have recently been intensively investigated, and improved thermoelectric performances (TEPs) have been observed in the materials doped with Ti [10-12] and Hf [13,14]. The relative abundance of the constituent elements in the earth's crust makes NbFeSb-

based materials very promising because of their low cost and mass production compatibility.

Recently, the TEP of NbFeSb-based materials has been considerably enhanced using the “diagonal-rule” doping technique, achieving a maximum figure of merit (zT_{max}) of ~ 1.5 at 1200 K for $\text{Nb}_{1-x}\text{Hf}_x\text{FeSb}$ [13]. Ti doping of NbFeSb provided the first breakthrough of TEP enhancement, resulting in a 25% increase in power factor for $\text{Nb}_{0.6}\text{Ti}_{0.4}\text{FeSb}_{0.95}\text{Sn}_{0.05}$ [10]. Further optimization of the sintering temperature yielded a massive power factor of $106 \mu\text{W cm}^{-1} \text{K}^{-2}$ at 300 K for $\text{Nb}_{0.95}\text{Ti}_{0.05}\text{FeSb}$ and a high maximum zT of 1.1 at 973 K for $\text{Nb}_{0.8}\text{Ti}_{0.2}\text{FeSb}$ [12]. These major achievements proved that Hf and Ti are excellent *p*-type dopants for NbFeSb. One of their secondary functions is to decrease lattice thermal conductivity (κ_{lat}) by enhancing phonon scattering [11-14]. Among the *p*-type dopants (Hf, Ti, and Zr), Hf exhibited the best advantages for TEP enhancement [15,16]; however, its rarity and high cost limit its practical applications.

Another traditional strategy used for band engineering and the suppression of thermal conductivity is alloying NbFeSb with isoelectronic elements. Fu et al. investigated the sub-

-주성재 · 김봉서 · 민복기: 책임연구원, 손지희 · 장정인: 연구지원원
*Corresponding Author: Sung-Jae Joo
[Tel: +82-55-280-1627, E-mail: sj_joo@keri.re.kr]
Copyright © The Korean Institute of Metals and Materials

stitution of V with Nb in VFeSb and reported a 55% reduction in the thermal conductivity of $V_{0.6}Nb_{0.4}FeSb$ compared with that of VFeSb [17]. In addition, the same group recently revealed that Ta alloying had the same effect of lowering the κ_{lat} while keeping electrical properties almost unchanged, achieving a maximum zT of 1.6 at 1200 K at the optimal compositions [18]. Farahi et al. fabricated $Nb_{0.88-x}Hf_{0.12}Ta_x-FeSb$ ($0 \leq x \leq 0.15$) samples and observed a ~28% reduction in the κ_{lat} of the $Nb_{0.73}Hf_{0.12}Ta_{0.15}FeSb$ sample at 350 K compared with the Ta-free sample [19]. The common reason for the decrease in κ_{lat} in the aforementioned experiments was the enhancement of point defect scattering due to fluctuations in atomic mass and strain field by Ta alloying.

In this study, NbFeSb samples codoped with Ti, Zr, and Sn were synthesized and the effects of V alloying on the TEP of $Nb_{0.8-x}V_xTi_{0.15}Zr_{0.05}FeSb_{0.98}Sn_{0.02}$ ($x = 0, 0.05, 0.1, 0.2, \text{ and } 0.3$) samples analyzed. The main goal of this study is to maximize the TEP of Hf-free NbFeSb materials by fully exploiting the concepts of diagonal-rule doping and isoelectronic alloying. V alloying has a definite effect, simultaneously reducing the power factor and thermal conductivity, even with a small V content. Thus, TEP degrades when the V content exceeds an optimum quantity. However, the addition of V may be advantageous at low x values by suppressing κ_{lat} , as evidenced by the maximum zT of 0.89 obtained for $Nb_{0.75}V_{0.05}Ti_{0.15}Zr_{0.05}Sn_{0.98}Sb_{0.02}$ at 973 K.

2. EXPERIMENTAL DETAILS

Elemental sources of Nb (99.95%, 3.175-mm diameter \times 3.175-mm length slug, Alfa Aesar), Fe (99.99%, 3.2–6.4-mm pieces, Alfa Aesar), Ti (99.98%, 3.175-mm diameter \times 3.175-mm length slug, Alfa Aesar), Zr (99.8% metal basis excluding Hf, 3–6-mm lump, Alfa Aesar), V (99.8% metal basis, 3.175-mm diameter \times 3.175-mm length slug, Alfa Aesar), Sn (99.999%, 2–3-mm grains, Kojundo), and Sb (99.999%, 2-mm grains, Kojundo) were used to synthesize the $Nb_{0.8-x}V_xTi_{0.15}Zr_{0.05}FeSb_{0.98}Sn_{0.02}$ ($x = 0, 0.05, 0.1, 0.2, \text{ and } 0.3$) HH compounds. The raw materials were weighed according to the stoichiometric composition, sealed in a quartz tube under Ar atmosphere, and melted completely using homemade radio frequency induction heating equipment. The melted material was immediately dipped into

water for quenching, crushed manually into smaller pieces, and vacuum-sealed in a quartz tube for annealing at 1173 K for 2 d. Subsequently, the annealed materials were ball-milled at 300 RPM (PM-100, Retsch) into powder and sieved to remove large particles ($\geq 45 \mu\text{m}$). The obtained fine powders were loaded into a graphite mold (12.7-mm diameter) and sintered using spark plasma-sintering equipment (Dr. Sinter, Fuji Electronic Industrial) at 1223 K for 10 min under a pressure of 65 MPa. The sintered ingots were cut into various sizes to measure their electrical conductivity (σ), Seebeck coefficient (S), thermal diffusivity (a), and specific heat capacity (C_p).

The sample phases were identified using X-ray diffractometry (XRD, $CuK\alpha$, X'Pert PRO MPD, Panalytical), and the microstructural features were observed via field-emission scanning electron microscopy (FE-SEM, Mira-II, Tescan). Furthermore, phase identification and the statistical analysis of grain maps were performed using electron backscatter diffraction (EBSD, TSL Hikari XP). The electrical resistivity (ρ) and S were simultaneously measured using a commercial system (ZEM-3, Ulvac-Riko). A differential scanning calorimeter (DSC 404C, Netzsch) and a laser flash measurement system (LFA-457, Netzsch) were used to measure the C_p and a , respectively, of the samples. The density (d) of the samples was measured using Archimedes' method. Based on the obtained parameters, the thermal conductivity, κ , was calculated as $\kappa = aC_p d$. The carrier concentration of the HH samples was obtained by performing a Hall effect measurement at 300 K under a magnetic field intensity of 9 T using a commercial physical property measurement system (Quantum Design).

3. RESULTS AND DISCUSSION

Figure 1(a) shows the XRD patterns of the sintered $Nb_{0.8-x}V_xTi_{0.15}Zr_{0.05}FeSb_{0.98}Sn_{0.02}$ samples. All the major peaks are indexed according to the reference pattern of NbFeSb (ICSD ID: 83928). No noticeable peaks attributed to impurity phases are observed within the XRD limit of detection. The lattice constants of samples with different V content are calculated from the position of the (220) peaks, which are plotted in Figure 1(b). As the nominal V content increases, the lattice constant decreases monotonically from

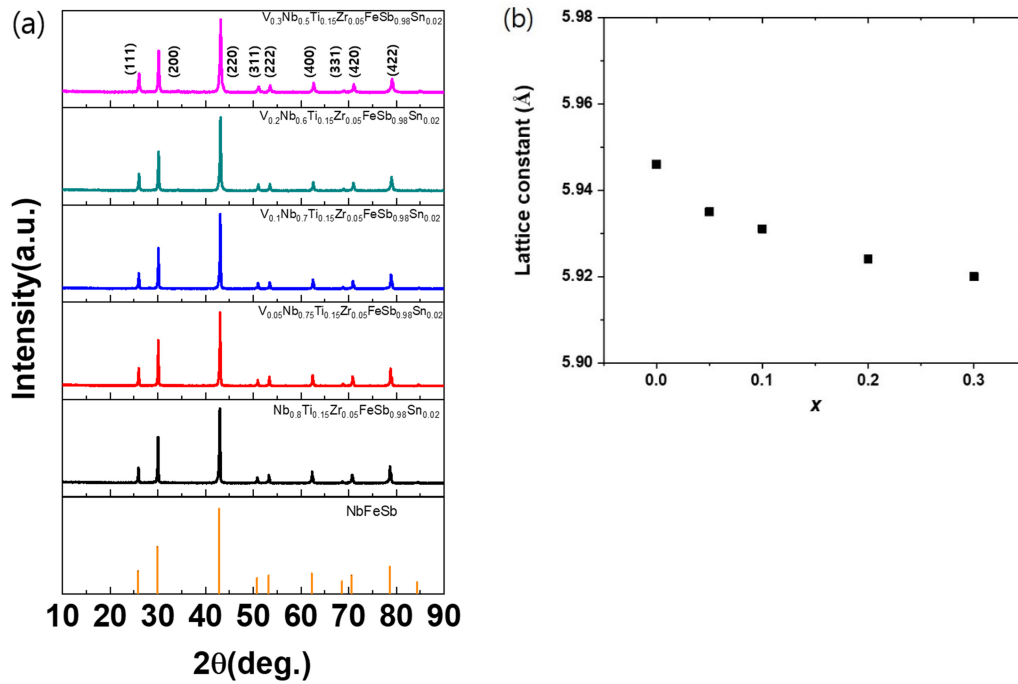


Fig. 1. (a) X-ray diffraction patterns and (b) lattice constants of the $\text{Nb}_{0.8-x}\text{V}_x\text{Ti}_{0.15}\text{Zr}_{0.05}\text{FeSb}_{0.98}\text{Sn}_{0.02}$ ($x = 0, 0.05, 0.1, 0.2,$ and 0.3) samples.

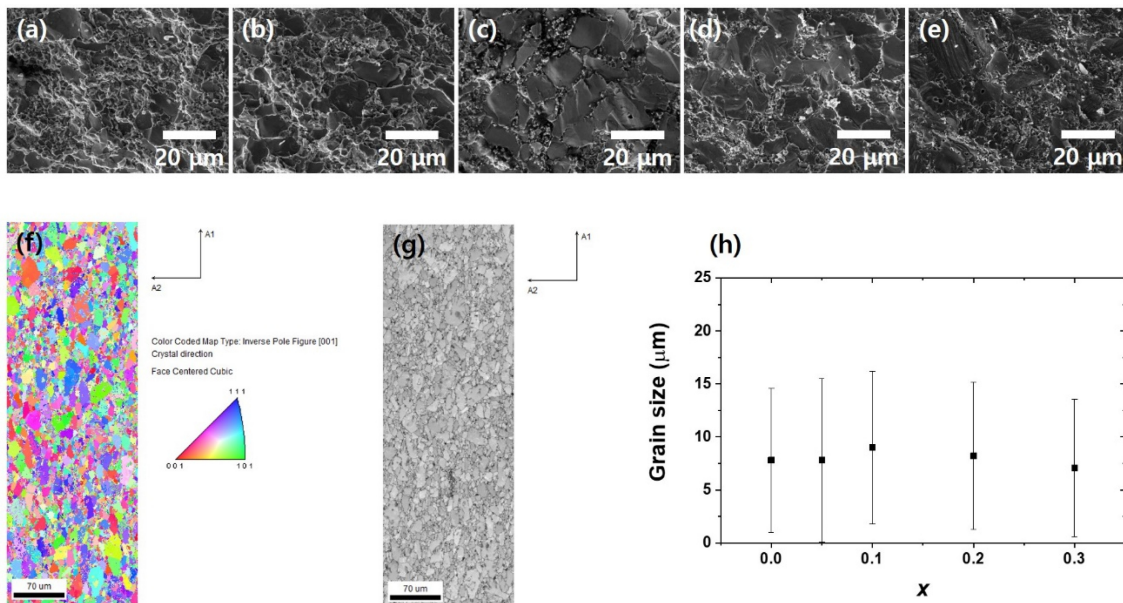


Fig. 2. (a)–(e) FE-SEM images of the fractured surfaces of the $\text{Nb}_{0.8-x}\text{V}_x\text{Ti}_{0.15}\text{Zr}_{0.05}\text{FeSb}_{0.98}\text{Sn}_{0.02}$ ($x = 0, 0.05, 0.1, 0.2,$ and 0.3) samples, respectively. (f) Inverse pole figure image obtained along the [001] direction, and (g) grain map of the $\text{Nb}_{0.7}\text{V}_{0.1}\text{Ti}_{0.15}\text{Zr}_{0.05}\text{FeSb}_{0.98}\text{Sn}_{0.02}$ sample. (h) Graph of the average grain size of the $\text{Nb}_{0.8-x}\text{V}_x\text{Ti}_{0.15}\text{Zr}_{0.05}\text{FeSb}_{0.98}\text{Sn}_{0.02}$ samples versus the V content, which was extracted statistically using the EBSD analysis.

5.946 ($x = 0$) to 5.920 Å ($x = 0.3$) because V (135 pm) has a smaller atomic radius than Nb (145 pm) [20].

Figures 2(a)–(e) show the microscopic morphology of the fractured surfaces of the $\text{Nb}_{0.8-x}\text{V}_x\text{Ti}_{0.15}\text{Zr}_{0.05}\text{FeSb}_{0.98}\text{Sn}_{0.02}$

samples, which were observed using FE-SEM. Large grains with diameters of >10 μm are mixed with small grains, and all samples exhibit various grain sizes. EBSD was used for a more detailed microstructural analysis, and Figures 2(f) and 2(g)

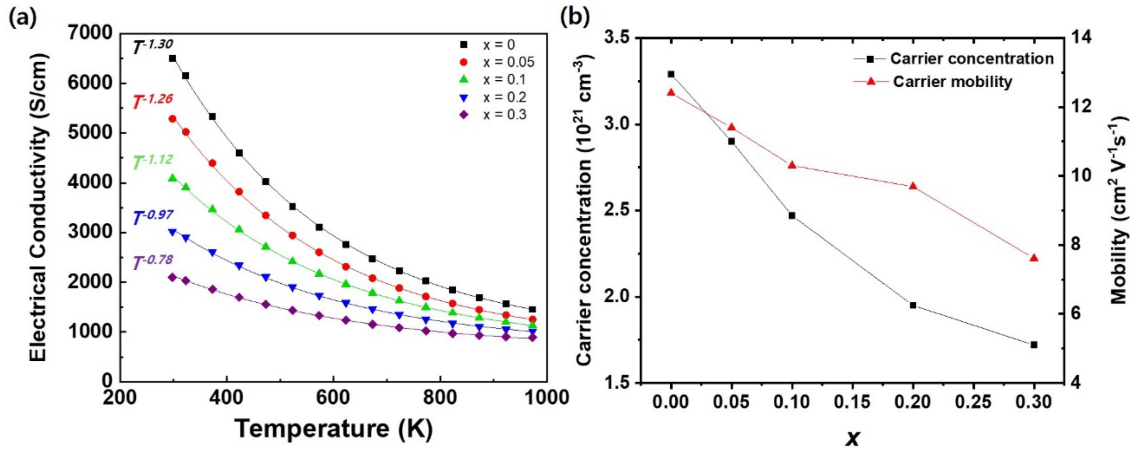


Fig. 3. (a) Temperature dependence of electrical conductivity, and (b) carrier concentration and mobility versus x of the $\text{Nb}_{0.8-x}\text{V}_x\text{Ti}_{0.15}\text{Zr}_{0.05}\text{FeSb}_{0.98}\text{Sn}_{0.02}$ ($x = 0, 0.05, 0.1, 0.2, \text{ and } 0.3$) samples.

show the inverse pole figure image along the [001] direction and the grain map of the $\text{Nb}_{0.7}\text{V}_{0.1}\text{Ti}_{0.15}\text{Zr}_{0.05}\text{FeSb}_{0.98}\text{Sn}_{0.02}$ sample, respectively. The random distribution of the [001] pole and the wide-ranging grain sizes are visible in these results, from which the statistical data presented in Figure 2(h) were extracted. The data indicate that the average grain size is unrelated to the V content and the standard deviation is large in all the samples. In addition, two-dimensional maps of the constituent elements, which are not shown in this study, confirmed that the materials are homogeneous.

Figure 3(a) shows the σ of the $\text{Nb}_{0.8-x}\text{V}_x\text{Ti}_{0.15}\text{Zr}_{0.05}\text{FeSb}_{0.98}\text{Sn}_{0.02}$ samples over the temperature range of 298–973 K. The samples demonstrate a metallic conduction behavior in which electrical conductivity decreases with increasing temperature. The σ vs. T data points are well fitted with several exponential curves following the T^{-n} law, where the exponent n decreases from 1.30 ($x = 0$) to 0.78 ($x = 0.3$) as the V content increases. This behavior indicates that the carrier scattering mechanism changes gradually from acoustic phonon dominated to mixed scattering, reflecting the increasing effect of alloy scattering with the addition of V [12,13,15,21]. Figure 3(b) shows the plots of the carrier concentration and mobility at 300 K as functions of the V content. The carrier concentration of the V-free sample is $3.3 \times 10^{21} \text{ cm}^{-3}$, and it decreases monotonically to $1.7 \times 10^{21} \text{ cm}^{-3}$ at $x = 0.3$, with a similar trend in carrier mobility.

The decreasing carrier concentration with increasing V content can be understood based on previous reports showing

that pure VFeSb is n type [22,23] and a certain amount of Ti is required to transform n -type VFeSb into a p -type material [22–25]. Thus, a part of the p -type dopants is consumed for compensation in VFeSb, which lowers the concentration of active dopants available to produce the major carriers, i.e., holes. Furthermore, the reduced solubility and doping efficiency of the Zr and Ti dopants with increasing V content has been reported to be one of the origins of the decreasing carrier concentration [26]. The reduction in carrier mobility with the addition of V is attributed to the combined effect of alloy scattering {Figure 3(a)} and the larger band effective mass of the hole in VFeSb versus in NbFeSb [11,26].

Figure 4(a) presents a comparison of the S of the $\text{Nb}_{0.8-x}\text{V}_x\text{Ti}_{0.15}\text{Zr}_{0.05}\text{FeSb}_{0.98}\text{Sn}_{0.02}$ samples from 298 to 973 K. Overall, S increases with x over the entire temperature range when $x \leq 0.1$. The maximum S (S_{max}) was observed at the highest measurement temperature of 973 K, reaching $186.7 \mu\text{V K}^{-1}$ in the sample with $x = 0.1$. However, as x increases further, S_{max} decreases and shows a maximum value at <973 K, as observed at $x = 0.3$. This is because VFeSb has a narrower bandgap (E_g) than NbFeSb [11,22,23], which is related to S_{max} according to the approximate equation $|S_{max}| \gg E_g / (2eT_{max})$ [27]. Here, T_{max} is the temperature at which $|S|$ is maximized. As E_g decreases with the addition of V, the excitation of thermally activated minority carriers across the bandgap is promoted at low temperatures. Consequently, bipolar conduction becomes non-negligible, causing $|S|$ to saturate and begin to decrease at low temperatures.

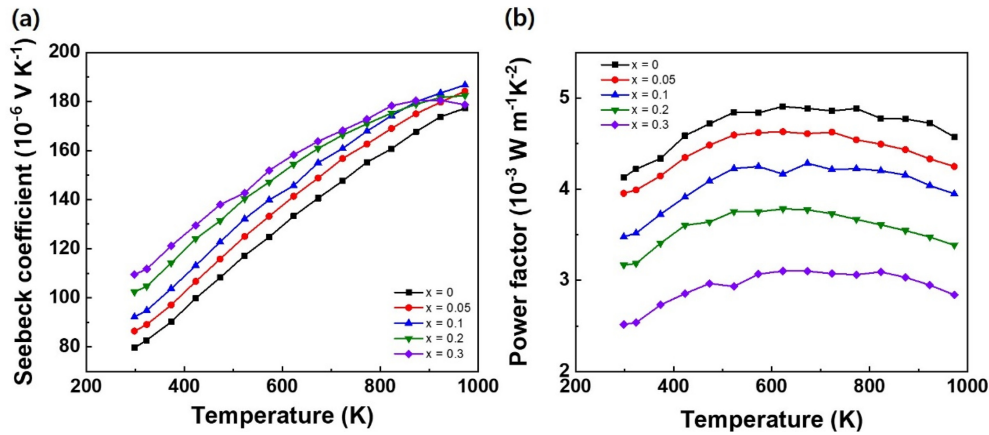


Fig. 4. Temperature dependence of the (a) Seebeck coefficient and (b) power factor of the $\text{Nb}_{0.8-x}\text{V}_x\text{Ti}_{0.15}\text{Zr}_{0.05}\text{FeSb}_{0.98}\text{Sn}_{0.02}$ ($x = 0, 0.05, 0.1, 0.2,$ and 0.3) samples.

Figure 4(b) shows the power factor (PF) calculated using the formula $PF = \sigma S^2$. The V-free sample has the highest PF , and almost constant values of $4.85\text{--}4.90 \text{ mW m}^{-1}\text{K}^{-2}$ are obtained in the temperature range of $523\text{--}773 \text{ K}$. By comparison, the V-added samples show increasingly smaller values of PF as the V content increases, due to the reduced σ . The decrease in PF_{max} is inversely proportional to x and reduces by $\sim 37\%$ at $x = 0.3$. These results suggest that the substitution of Nb with V is not advantageous in terms of PF .

Meanwhile, Figure 5(a) clearly indicates that the addition of V reduces thermal conductivity. Thermal conductivity (κ) decreases with temperature in all the samples, and the maximum κ (κ_{max}) is observed at 298 K . The κ_{max} of the V-free sample is $\sim 10.1 \text{ W K}^{-1}\text{m}^{-1}$. However, adding a small V content causes a considerable decrease in κ_{max} , as seen in the $\text{Nb}_{0.75}\text{V}_{0.05}\text{Ti}_{0.15}\text{Zr}_{0.05}\text{FeSb}_{0.98}\text{Sn}_{0.02}$ sample, whose κ_{max} was reduced by $\sim 17.5\%$ to a value of $8.33 \text{ W K}^{-1}\text{m}^{-1}$. A more dramatic reduction in κ_{max} was observed in the V-rich samples, and the κ_{max} value of the $\text{Nb}_{0.5}\text{V}_{0.3}\text{Ti}_{0.15}\text{Zr}_{0.05}\text{FeSb}_{0.98}\text{Sn}_{0.02}$ sample was reduced by more than 50% to $\sim 4.93 \text{ W K}^{-1}\text{m}^{-1}$ by V alloying. Notably, κ comprises three components—contributions from the lattice (κ_{lat}), majority carrier (κ_{el}), and bipolar conduction (κ_{bi}). Therefore, an independent estimation of each component is required to establish a fair comparison of the κ_{lat} values of the samples.

First, κ_{bi} can be ignored considering the extremely high majority carrier concentrations {Figure 3(b)}, and κ_{el} is calculated by applying the Wiedemann–Franz law:

$$\kappa_{el} = L\sigma T, \quad (1)$$

where L denotes the Lorenz number. When a single parabolic band model is assumed, the S and Lorenz number are calculated using Fermi–Dirac integrals $F_n(\xi)$ as follows [28]:

$$S = \pm \frac{k_B}{e} \left\{ \frac{\left(r + \frac{5}{2}\right) F_{r+\frac{3}{2}}(\xi)}{\left(r + \frac{3}{2}\right) F_{r+\frac{1}{2}}(\xi)} - \xi \right\}, \quad (2)$$

$$L = \left(\frac{k_B}{e}\right)^2 \left\{ \frac{\left(r + \frac{7}{2}\right) F_{r+\frac{5}{2}}(\xi)}{\left(r + \frac{3}{2}\right) F_{r+\frac{1}{2}}(\xi)} - \left[\frac{\left(r + \frac{5}{2}\right) F_{r+\frac{3}{2}}(\xi)}{\left(r + \frac{3}{2}\right) F_{r+\frac{1}{2}}(\xi)} \right]^2 \right\}, \quad (3)$$

$$F_n(\xi) = \int_0^\infty \frac{x^n}{1 + e^{x-\xi}} dx, \quad (4)$$

where r and ξ denote the scattering parameters and the reduced Fermi energy, E_F/kT , respectively. We calculated L and then subtracted the calculated κ_{el} to obtain the lattice thermal conductivity, κ_{lat} , as shown in Figure 5(b). The dependence of κ_{lat} on temperature is the same as that of κ shown in Figure 5(a); however, κ_{lat} decreases with increasing V content until $x = 0.2$, above which κ_{lat} remains almost unchanged. In the $\text{Nb}_{0.6}\text{V}_{0.2}\text{Ti}_{0.15}\text{Zr}_{0.05}\text{FeSb}_{0.98}\text{Sn}_{0.02}$ sample, the κ_{max} at 298 K decreased by $\sim 36\%$ compared with the κ_{max} of the V-free sample, whereas the difference between the κ_{lat} values decreases at higher temperatures.

Figure 6 shows zT and summarizes the total effects of V addition. Based on the results of this study, the samples with

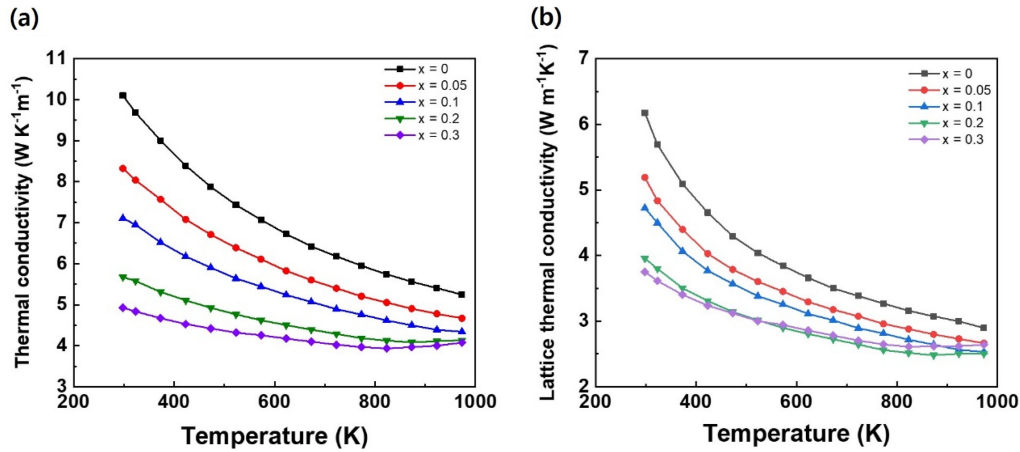


Fig. 5. Temperature dependence of (a) thermal conductivity and (b) lattice thermal conductivity of the $\text{Nb}_{0.8-x}\text{V}_x\text{Ti}_{0.15}\text{Zr}_{0.05}\text{FeSb}_{0.98}\text{Sn}_{0.02}$ ($x = 0, 0.05, 0.1, 0.2,$ and 0.3) samples.

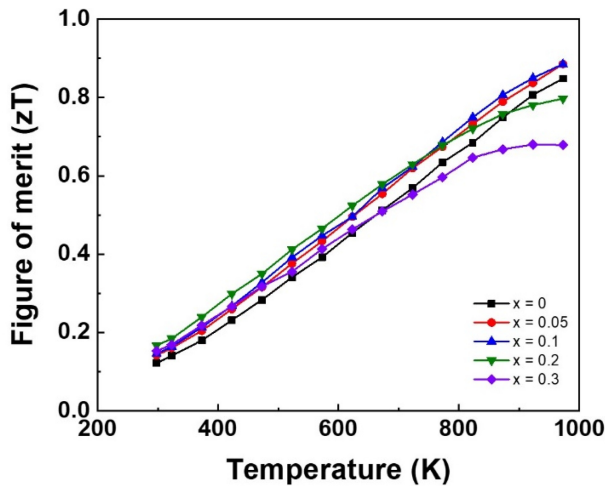


Fig. 6. Temperature dependence of zT for the $\text{Nb}_{0.8-x}\text{V}_x\text{Ti}_{0.15}\text{Zr}_{0.05}\text{FeSb}_{0.98}\text{Sn}_{0.02}$ ($x = 0, 0.05, 0.1, 0.2,$ and 0.3) samples.

$x < 0.1$ had a higher zT s than those of the V-free sample over the entire temperature range. The maximum zT value of 0.89 was observed in the $\text{Nb}_{0.75}\text{V}_{0.05}\text{Ti}_{0.15}\text{Zr}_{0.05}\text{FeSb}_{0.98}\text{Sn}_{0.02}$ and $\text{Nb}_{0.7}\text{V}_{0.1}\text{Ti}_{0.15}\text{Zr}_{0.05}\text{FeSb}_{0.98}\text{Sn}_{0.02}$ samples at 973 K, which is $\sim 5\%$ higher than that of the V-free $\text{Nb}_{0.8}\text{Ti}_{0.15}\text{Zr}_{0.05}\text{FeSb}_{0.98}\text{Sn}_{0.02}$ sample. Although the improvement is insignificant, we believe that a small V content can still be used to fine-tune NbFeSb-based thermoelectric materials.

4. CONCLUSIONS

The effect of V alloying on TEP was investigated in this study using Hf-free HH alloys $\text{Nb}_{0.8-x}\text{V}_x\text{Ti}_{0.15}\text{Zr}_{0.05}\text{FeSb}_{0.98}\text{Sn}_{0.02}$

($x = 0, 0.05, 0.1, 0.2,$ and 0.3). The carrier concentration and mobility reduced when V was substituted for Nb, and the lattice thermal conductivity decreased substantially even with a small V content. Notably, the addition of V reduces κ_{lat} even when the materials are already codoped with Ti, Zr, and Sn, which effectively function as phonon scattering centers. Furthermore, a maximum zT value of 0.89 was obtained for $\text{Nb}_{0.75}\text{V}_{0.05}\text{Ti}_{0.15}\text{Zr}_{0.05}\text{Sn}_{0.98}\text{Sb}_{0.02}$ at 973 K by adding V.

ACKNOWLEDGMENT

This research was supported by the Korea Electrotechnology Research Institute Primary research program through the National Research Council of Science & Technology (NST), which is funded by the Ministry of Science and ICT (MSIT) (Code number 22A01023).

Conflict of Interest

The authors have no conflicts of interest to declare.

REFERENCES

1. G. Rogl, A. Grytsiv, P. Rogl, N. Peranio, E. Bauer, M. Zehetbauer, and O. Eibl, *Acta Mater.* **63**, 30 (2014).
2. S.H. Bae, K.H. Lee, and S.-M. Choi, *Intermetallics* **105**, 44 (2019).
3. Y.-E. Cha and I.-H. Kim, *Korean J. Met. Mater.* **57**, 801 (2019).

4. J. de Boor, T. Dasgupta, U. Saparamadu, E. Müller, and Z.F. Ren, *Mater. Today Energy* **4**, 105 (2017).
5. W.-D. Liu, Z.-G. Chen, and J. Zou, *Adv. Energy Mater.* **8**, 1800056 (2018).
6. I.-J. Lee, S.-B. Park, S.-C. Ur, K.-W. Jang, and I.-H. Kim, *Korean J. Met. Mater.* **57**, 264 (2019).
7. S.J. Poon, *J. Phys. D: Appl. Phys.* **52**, 493001 (2019).
8. J. Yu, Y. Xing, C. Hu, Z. Huang, Q. Qiu, C. Wang, K. Xia, Z. Wang, S. Bai, X. Zhao, L. Chen, and T. Zhu, *Adv. Energy Mater.* **10**, 2000888 (2020).
9. S. Chen and Z. Ren, *Mater. Today* **16**, 387 (2013).
10. G. Joshi, R. He, M. Engber, G. Samsonidze, T. Pantha, E. Dahal, K. Dahal, J. Yang, Y. Lan, B. Kozinsky, and Z. Ren, *Energy Environ. Sci.* **7**, 4070 (2014).
11. C. Fu, T. Zhu, Y. Liu, H. Xie, and X. Zhao, *Energy Environ. Sci.* **8**, 216 (2015).
12. R. He, D. Kraemer, J. Mao, L. Zeng, Q. Jie, Y. Lan, C. Li, J. Shuai, H.S. Kim, Y. Liu, D. Broido, C.W. Chu, G. Chen, and Z. Ren, *Proc. Natl. Acad. Sci. U S A* **113**, 13576 (2016).
13. C. Fu, S. Bai, Y. Liu, Y. Tang, L. Chen, X. Zhao, and T. Zhu, *Nat. Commun.* **6**, 8144 (2015).
14. J. Shen, C. Fu, Y. Liu, X. Zhao, and T. Zhu, *Energy Storage Mater.* **10**, 69 (2018).
15. W. Ren, H. Zhu, Q. Zhu, U. Saparamadu, R. He, Z. Liu, J. Mao, C. Wang, K. Nielsch, Z. Wang, and Z. Ren, *Adv. Sci.* **5**, 1800278 (2018).
16. S. Bhattacharya and G.K.H. Madsen, *J. Mater. Chem. C* **4**, 11261 (2016).
17. C. Fu, H. Xie, T.J. Zhu, J. Xie, and X.B. Zhao, *J. Appl. Phys.* **112**, 124915 (2012).
18. J. Yu, C. Fu, Y. Liu, K. Xia, U. Aydemir, T.C. Chasapis, G.J. Snyder, X. Zhao, and T. Zhu, *Adv. Energy Mater.* **8**, 1701313 (2018).
19. N. Farahi, C. Stiewe, D.Y.N. Truong, Y. Shi, S. Salamon, J. Landers, B. Eggert, H. Wende, J.D. de Boor, H. Kleinke, and E. Müller, *ACS Appl. Energy Mater.* **2**, 8244 (2019).
20. J.C. Slater, *J. Chem. Phys.* **41**, 3199 (1964).
21. J. Shuai, J. Mao, S. Song, Q. Zhu, J. Sun, Y. Wang, R. He, J. Zhou, G. Chen, D.J. Singh, and Z. Ren, *Energy Environ. Sci.* **10**, 799 (2017).
22. D.P. Young, P. Khalifah, R.J. Cava, and A.P. Ramirez, *J. Appl. Phys.* **87**, 317 (2000).
23. L. Jodin, J. Tobola, P. Pecheur, H. Scherrer, and S. Kaprzyk, *Phys. Rev. B* **70**, 184207 (2004).
24. R. Hasan and S.C. Ur, *Electron. Mater. Lett.* **14**, 725 (2018).
25. M. Zou, J.F. Li, and T. Kita, *J. Solid State Chem.* **198**, 125 (2013).
26. C. Fu, Y. Liu, X. Zhao, and T. Zhu, *Adv. Electron. Mater.* **2**, 1600394 (2016).
27. H.J. Goldsmid and J.W. Sharp, *J. Electron. Mater.* **28**, 869 (1999).
28. H.J. Goldsmid, *Introduction to thermoelectricity*. Springer-Verlag Berlin Heidelberg (2010).